Lipid bilayer and cytoskeletal interactions in a red blood cell

Zhangli Peng[a], Xuejin Li[b], Igor V. Pivkin[c,d], Ming Dao[a], George E. Karniadakis[b], and Subra Suresh[e,1]

[a]Department of Materials Science and Engineering, Massachusetts Institute of Technology, Cambridge, MA 02139; [b]Division of Applied Mathematics, Brown University, Providence, RI 02912; [c]Institute of Computational Science, Faculty of Informatics, University of Lugano, 6904 Lugano, Switzerland; [d]Swiss Institute of Bioinformatics, 1015 Lausanne, Switzerland; and [e]Department of Materials Science and Engineering and Department of Biomedical Engineering, Carnegie Mellon University, Pittsburgh, PA 15213

We study the biomechanical interactions between the lipid bilayer and the cytoskeleton in a red blood cell (RBC) by developing a general framework for mesoscopic simulations. We treated the lipid bilayer and the cytoskeleton as two distinct components and developed a unique whole-cell model of the RBC, using dissipative particle dynamics (DPD). The model is validated by comparing the predicted results with measurements from four different and independent experiments. First, we simulated the micropipette aspiration and quantified the cytoskeletal deformation. Second, we studied the membrane fluctuations of healthy RBCs and RBCs parasitized to different intraerythrocytic stages by the malaria-inducing parasite *Plasmodium falciparum*. Third, we subjected the RBC to shear flow and investigated the dependence of its tank-treading frequency on shear rate. Finally, we simulated the bilayer–cytoskeletal detachment in channel flow to quantify the strength of such interactions when the corresponding bonds break. Taken together, these experiments and corresponding systematic DPD simulations probe the governing constitutive response of the cytoskeleton, elastic stiffness, viscous friction, and strength of bilayer–cytoskeletal interactions as well as membrane viscosities. Hence, the DPD simulations and comparisons with available independent experiments serve as validation of the unique two-component model and lead to useful insights into the biomechanical interactions between the lipid bilayer and the cytoskeleton of the RBC. Furthermore, they provide a basis for further studies to probe cell mechanistic processes in health and disease in a manner that guides the design and interpretation of experiments and to develop simulations of phenomena that cannot be studied systematically by experiments alone.

coarse graining | worm-like chain | multiscale modeling | adhesion energy | erythrocyte

The red blood cell (RBC) membrane consists of two components: a lipid bilayer and an attached 2D spectrin network that acts as the cytoskeleton. The resistance of the lipid bilayer to bending is controlled by the bending rigidity, k_c, whereas the spectrin network's resistance to shear strain is characterized by the in-plane shear modulus, μ_s. Under normal conditions, the cytoskeleton is tightly attached to the lipid bilayer from the cytoplasmic side. However, under certain pathological conditions, e.g., in sickle cell disease, the cytoskeleton may become dissociated from the lipid bilayer (1). Although the biomechanics of the two-component erythrocyte membrane have been studied extensively for decades (2), the mechanical properties of the interactions between the lipid bilayer and the cytoskeleton (such as elastic stiffness, viscous friction, and strength) via the pinning connections of transmembrane proteins are still largely unknown. This is at least in part ascribed to the fact that it is difficult to measure these interactions directly from experiments, because the length scale of these connections is too small compared with the characteristic length scale of the cell mechanical experiments.

The mechanical properties associated with the bilayer–cytoskeletal interactions strongly influence biorheology, erythrocyte function, and the onset and advancement of RBC diseases (3). For example, it has been hypothesized that the pathogenesis of hereditary spherocytosis is related to the weakened bilayer–cytoskeletal interaction strength, which leads to reduced spectrin density, and the loss of bilayer membrane resulting in reduced surface area (4). In addition, in sickle cell disease, the detachment of the RBC lipid bilayer from the spectrin network owing to hemoglobin polymerization also causes "budding off" of the bilayer, which in turn results in reduced cell deformability (1). Furthermore, when the RBCs pass through the interendothelial slits in the spleen, they undergo severe deformation. Here, the biophysical properties mediated by the bilayer–cytoskeletal interactions may play a significant role in the ensuing mechanical filtering process (5, 6).

Several computational approaches, including continuum formulations and particle-based numerical models, have been developed recently and applied to RBC simulations at different length scales; a review of these approaches can be found in ref. 7. These models may quantitatively mimic the mechanical properties of healthy and pathological RBCs under select experimental conditions and stress states. However, they do not lend themselves to detailed whole-cell investigations of a wide variety of biophysical problems involving the RBCs, such as the aforementioned issues of bilayer–cytoskeletal detachment or bilayer loss in hereditary spherocytosis due to defective protein attachments. In existing whole-cell models, the membrane is usually considered as a single-component shell with effective properties (8–10) that seek to estimate the combined effects of the lipid bilayer and the spectrin network. In situations where two-component molecular models have been invoked, the computational cost is prohibitively high, such that usually only a small portion of the cell membrane is modeled, a consequence of which is that the whole-cell response is not adequately and efficiently captured (11). Furthermore, such models are computationally too inefficient to be amenable to blood microrheology studies involving large numbers of RBCs in flow. For these reasons, there is a compelling need to develop a unique two-component, particle-based, whole-cell model to study the biophysics of RBCs arising from the interactions between the lipid bilayer and the spectrin cytoskeletal network. Such a model would provide a more reliable method and an overall modeling framework to extract mechanical properties of RBCs from a variety of independent experimental methods.

Currently there are no experimental techniques that directly measure the mechanical characteristics of the bilayer–cytoskeletal

interactions. The specific characteristics of these interactions influence, in different ways, the mechanical property data inferred from several different experiments, such as micropipette aspiration and vesiculation (12, 13), membrane thermal fluctuations (14–16), tank-treading motion (17), and tethering of the lipid bilayer in channel flow (18). In the present study, we investigate the effects of the bilayer–cytoskeletal interactions in these experiments, using a unique two-component mesoscale RBC model implemented in dissipative particle dynamics (DPD).

Results and Discussion

We use the DPD formulation to develop the two-component model by extending the one-component RBC membrane model (19). This unique two-component model is capable of incorporating elastic and shear energy of the lipid bilayer and the cytoskeleton separately. In addition, we include both the normal and the tangential interactions between the lipid bilayer and the cytoskeleton as well as the membrane viscosities. This two-component mesoscale RBC model can also be implemented in conjunction with other methods such as the lattice Boltzmann method (20) and multiparticle collision dynamics (21). In this unique two-component RBC model, the membrane is modeled with two different components, i.e., the lipid bilayer and the cytoskeleton. Specifically, each component is composed of a 2D triangulated network with N_v vertices, where each vertex is represented by a DPD particle. In most simulations, we use $N_v = 23,867$ so that each DPD particle on the triangulated network of the cytoskeleton represents a junctional complex in the RBC spectrin network (9). In contrast to the one-component DPD model, the lipid bilayer of the two-component model has no shear stiffness, but only bending stiffness and a very large local area stiffness. Similarly, the cytoskeleton has no bending stiffness, but possesses a large shear stiffness. Further details of the model are provided in *Methods* and in *SI Text*. Parameters are listed in Table S1.

We probe the bilayer–cytoskeletal interactions by applying the two-component DPD model to simulate four independent experiments on RBCs: (*a*) fluorescence-marked micropipette aspiration (12), (*b*) membrane fluctuations (14), (*c*) tank-treading motion in shear flow (17), and (*d*) bilayer–cytoskeletal detachment in channel flow (18). Because only one or two mechanical parameters in each simulation of these four experiments are relevant to the result, our approach provides a good protocol in investigating the effects of these parameters in isolation, in a systematic and controlled manner while, at the same time, validating the two-component model.

Fluorescence-Marked Micropipette Aspiration. Using the two-component DPD model we are able to simulate, with the same set of input mechanical parameters, micropipette experiments that provide estimates of the area modulus (k_l shown in *SI Text*) of the lipid bilayer (22) as well as the area and shear moduli (k_s and μ_s shown in *SI Text*) of the cytoskeleton (12, 23). Such a simulation is not possible with the one-component model, in which the large local area modulus of the bilayer is absent. In micropipette aspiration, the local area modulus (k_l) of the lipid bilayer is measured as five orders higher (22) than the area or shear modulus (k_s or μ_s) of the cytoskeleton (12, 23). To investigate the effect of slip between the lipid bilayer and the cytoskeleton on deformation, we perform detailed numerical simulations of the fluorescence-marked micropipette aspiration of RBCs (12). To our knowledge, this is a unique experiment in which the slip between the lipid layer and the cytoskeleton as well as the local area deformation of the cytoskeleton was quantitatively obtained. Details of the setup of the micropipette aspiration simulation can be found in *SI Text*.

We use the two-component DPD model and compare the results with experimental data (12) and finite-element method (FEM) simulations (24) as shown in Fig. 1. We consider three cases in DPD simulations: $N_v = 23,867$ and $N_v = 5,000$ with a stress-free initial configuration and $N_v = 23,867$ with a prestressed initial
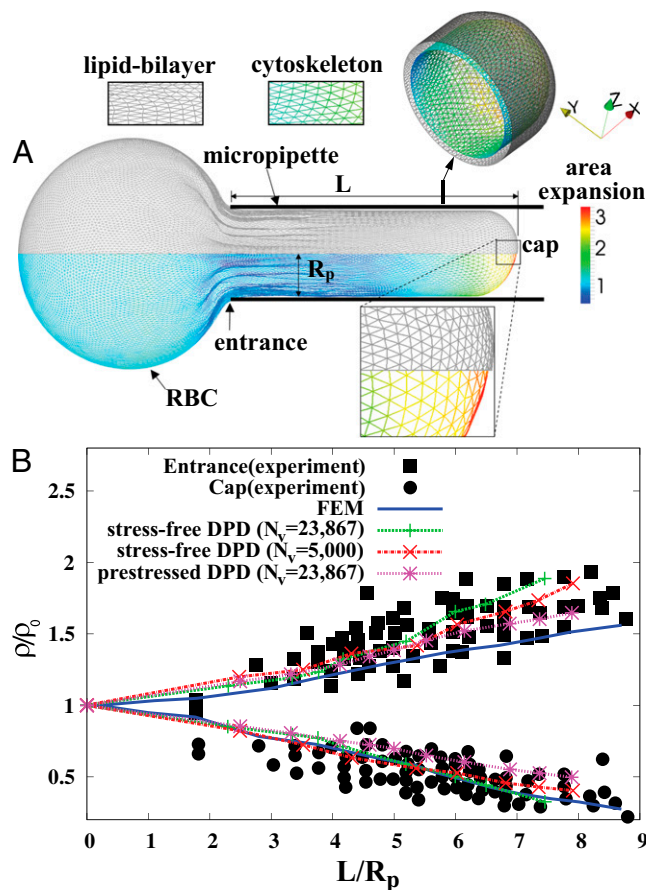
Fig. 1. Cytoskeletal area deformation during micropipette aspiration. (*A*) Simulated red blood cell in the micropipette. The gray triangular network is the lipid bilayer and the colored triangular network is the cytoskeleton. For clarity, only half of each triangular network is shown due to symmetry. The contour is the area deformation of the cytoskeleton. (*B*) Comparison of the two-component DPD model with the experiment (12) and the FEM model (24). The area expansion of the contour is defined as $\lambda_1 \cdot \lambda_2$, where λ_1 and λ_2 are the principal stretches. R_p is the pipette radius, ρ and ρ_0 are the current and initial protein densities in the cytoskeleton, L is the aspiration length under different pressures, and N_v is the number of DPD particles in each triangular network. Note that $\rho/\rho_0 = 1/(\lambda_1 \cdot \lambda_2)$.

configuration in which a negative isotropic stress $\overline{T} = -30$ pN/μm is applied in the cytoskeleton. The cytoskeleton density is higher in the DPD simulations than in the FEM simulation with the same prestress $\overline{T} = -30$ pN/μm in the cytoskeleton (24). The results of all three DPD simulation cases are in the range of experimental data, and the cytoskeleton deformation is smaller in the prestressed DPD case and the coarser DPD case with $N_v = 5,000$ as shown in Fig. 1*B*. The prestressed DPD case is closer to the FEM case in the entrance region, but the stress-free DPD case matches better with the FEM case in the cap region. The discrepancies may be due to the fact that the analysis of the deformation of individual spectrin molecules is performed in the DPD model with 23,867 DPD particles of the whole cell (25), whereas such details are absent in the FEM model. In addition to the cytoskeletal deformation, we are also able to quantify the maximum bilayer–cytoskeletal interaction force on one junctional complex (near the cap region) as 5.7 pN when $L/R_p = 12$. Such estimates of the interaction force between the lipid layer and the spectrin network provide valuable information about the vesiculation process in a micropipette (13). In vesiculation, detachment of the lipid bilayer from the cytoskeleton occurs due to the bilayer–cytoskeletal bond rupture during aspiration. In summary, the

two-component model allows us to simulate accurately both micropipette aspiration experiments of measuring bilayer area modulus and cytoskeletal moduli with the same set of parameters, hence quantifying the cytoskeletal deformation and estimating the bilayer–cytoskeleton interaction force directly at the molecular level in the micropipette aspiration; this cannot be achieved using existing models.

Membrane Fluctuations. Nanoscale fluctuations or "flickering" of RBCs have been studied theoretically and experimentally for decades (15, 26–30). Determining RBC membrane fluctuations provides a diagnostic capability to assess the health or pathological state of the whole RBC (14, 15). Membrane fluctuations experiments can probe the local mechanical properties of the lipid-bilayer membrane at different locations, such as central and rim regions, separately. This approach provides a noninvasive technique, in which the mechanical properties of the undeformed state are measured, whereas in micropipette aspiration the cell is subject to significant deformation.

The cell shape has a strong effect on the extent of thermal fluctuations (15), which, in turn, could be correlated with the healthy or pathological state of the cell. In addition, the interactions between the lipid bilayer and the cytoskeleton are usually simplified. For example, the cytoskeleton is often modeled as completely rigid (28), as a 3D network (31), or as a 2D Gaussian network (29). Friction and elastic interactions between the lipid bilayer and the cytoskeleton are usually ignored (30). Therefore, it is desirable to use whole-cell models to study thermal fluctuations with sufficient molecular details.

Recently, diffraction phase microscopy (DPM) has been used to map the instantaneous thickness of RBCs whereby nanometer levels of accuracy in the measurement of membrane fluctuations could be achieved at a temporal resolution of 1 ms (14, 15). In our previous work, the one-component DPD model was used to simulate healthy RBCs and RBCs parasitized to different intra-erythrocytic asexual stages by the malaria-inducing parasite *Plasmodium falciparum* (32). Although the simulation results from the one-component model match well with the fluctuations of healthy cells at room and normal physiological temperatures, they underestimate thermal fluctuations of RBC membranes for healthy RBCs at febrile temperature and ring stage malaria-infected RBCs, unless the bending stiffness is artificially reduced significantly (32).

Fig. 2*A* shows the full width at half maximum (FWHM) (32) of membrane fluctuations for a healthy RBC at the normal physiological temperature ($T \sim 37\,°C$) for different values of the bilayer–cytoskeletal elastic interaction coefficient k_{bs} and different levels of coarse graining with $N_v = 500$, 1,000 and 2,000, using the two-component model. The detailed simulation setup and coarse-graining procedure can be found in *SI Text*. We find that the amplitude of membrane fluctuations decreases with increased k_{bs} (Fig. 2*A*) and approaches a constant limiting value after k_{bs} reaches a critical value. This critical value of k_{bs} is smaller for the model with $N_v = 2{,}000$, because the limiting lower-bound value of amplitude with large k_{bs} is higher with $N_v = 2{,}000$ due to the finer resolution, so that it reaches this limiting value faster. It is also due to the fact that with the same value of k_{bs}, the effective elastic stiffness of a single junctional complex connection is larger with a higher resolution (*SI Text*). When k_{bs} is very large, there is a strong coupling between the bilayer and the cytoskeleton; i.e., they fluctuate as if they were one effective membrane, consistent with the analysis in ref. 33. If k_{bs} is small, the bilayer–cytoskeletal coupling is weak. In the extreme case where $k_{bs} = 0$, the amplitude of fluctuations is the same as that for a pure lipid bilayer. We also find that the FWHM value increases with finer DPD resolution but it is independent of the bilayer–cytoskeletal friction coefficient f_{bs}, cytoskeleton viscosity η_s, and bilayer viscosity η_b, in agreement with existing theoretical models (34).
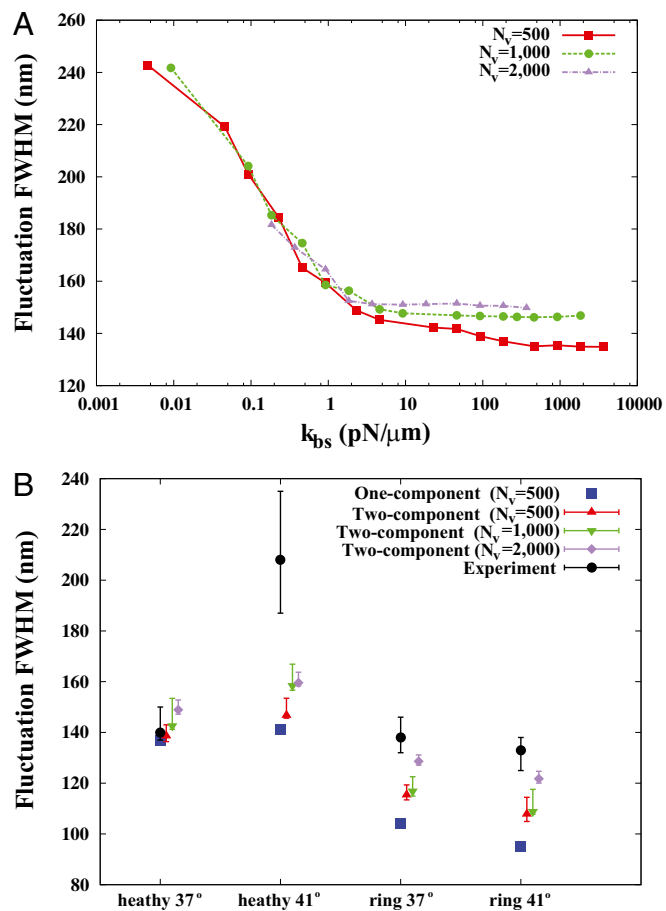
Fig. 2. Membrane fluctuations. (*A*) Effect of the bilayer–cytoskeletal interaction stiffness k_{bs} on the full width at half maximum (FWHM) (32) of membrane fluctuations for the case of healthy RBCs at the physiological temperature ($T \sim 37\,°C$), using two-component models with $N_v = 500$, 1,000, 2,000. (*B*) Comparison of FWHM from simulations and experiments for different stages of malaria-infected RBCs at the physiological temperature ($T \sim 37\,°C$) and the febrile temperature ($T \sim 41\,°C$). The simulations are conducted using different two-component models with $N_v = 500$, 1,000, 2,000. The error bars of the simulations are obtained using different values of k_{bs} (upper bound, $k_{bs} = 4.6$ pN/μm; midvalue, $k_{bs} = 46$ pN/μm; lower bound, $k_{bs} = 460$ pN/μm).

We compare our simulation results with experimental data and the one-component DPD model for healthy RBCs and RBCs parasitized to the ring stage (i.e., about 10–24 h following the invasion of the *P. falciparum* malaria parasite into the erythrocyte). These simulations for physiological ($T \sim 37\,°C$) and febrile ($T \sim 41\,°C$) temperatures are shown in Fig. 2*B*. The shear moduli of the RBC membrane for these different cases were measured experimentally in ref. 14, and they are shown in Table S2. The error bars of the simulations are obtained using different values of k_{bs} (upper bound, $k_{bs} = 4.6$ pN/μm; midvalue, $k_{bs} = 46$ pN/μm; lower bound, $k_{bs} = 460$ pN/μm), as the FWHM value increases with decreased k_{bs}. Fig. 2*B* shows that the results of the two-component DPD model are more consistent with the experimental data, especially with more DPD particles and at a smaller value of k_{bs}. This result shows that the bilayer–cytoskeletal elastic interaction coefficient k_{bs} indeed plays a key role in the thermal fluctuations experiments, and the discrepancy between the experimental data and the one-component RBC model can be significantly reduced by the two-component model.

Tank-Treading Motion of a RBC in Shear Flow. Next we simulate the motion of a RBC in shear flow, known to exhibit complex dynamic

behavior. This includes tank-treading (TT) motion, in which the RBC deforms to an ellipsoidal shape and the membrane circulates around while the inclination angle remains almost unchanged (35). An important characteristic of the TT dynamics of a RBC in shear flow is its frequency, i.e., the number of TT cycles per second. Although many experimental studies have been devoted to the measurement of TT frequency, considerable uncertainty exists with respect to the dependence of TT frequency (f) of RBCs on shear rate ($\dot{\gamma}$). For example, Fischer et al. (35) and Tran-Son-Tay et al. (36) found that f increases linearly with $\dot{\gamma}$. By contrast, Fischer (17) found that $f \sim \dot{\gamma}^{\beta}$ with the scaling exponent β between 0.85 and 0.95. Another fundamental question is the importance of apparent slip between the lipid bilayer and the cytoskeleton during the TT motion of a healthy or diseased RBC, e.g., in hereditary spherocytosis where the transmembrane protein density may be significantly reduced (37). Here, we simulate the TT motion of a RBC in a shear flow to investigate the correct functional relationship between f and $\dot{\gamma}$ and to quantify the effect of apparent slip by varying the bilayer–cytoskeletal friction. The detailed simulation setup and parameters can be found in *SI Text*.

Fig. 3*A* shows that the TT frequency f increases linearly with $\dot{\gamma}$ for RBCs in a narrow gap flow with gap width $H = 12$ μm in both one-component and two-component RBC models but nonlinearly when we increase the gap width to $H = 36$ μm. These results are consistent with the experimental findings in refs. 35 and 36 for small gaps and with Fischer (17) in the experiment with a wide gap. Specifically, we observe a nonlinear dependence $f \sim \dot{\gamma}^{\beta}$ with the exponent $\beta \simeq 0.91$ in both RBC models. When the RBC rotates in shear flow, the velocity field of fluid flow around the RBC changes significantly (38). In a narrow channel, the strong confinement induces a flow parallel to the channel walls, resulting in enhanced local shear stress around the RBC. In a wide channel, the influence of solid walls on the local flow field around the RBC is very small or even negligible. Thus, there is a decrease in f compared with that for the RBC in a narrow channel. The functional relationship between f and $\dot{\gamma}$ is similar for both the one-component and the two-component models, although the values of f for the latter are somewhat lower.

Next, we study the effect of the bilayer–cytoskeletal friction coefficient f_{bs} as shown in Fig. 3*B*. To this end, we define the angular trajectory θ of a marked particle either on the lipid bilayer or on the cytoskeleton as an angle between the position vector of marked particles and the flow direction as shown in Fig. 3*A, Inset*. Fig. 3*B* shows θ as a function of time for different cases with the same initial position. We find that when using the value of $f_{bs} = 0.194$ pN·μm^{-1}·s^{-1}, which is derived on the basis of experimentally measured diffusivities of transmembrane proteins and the fluctuation dissipation theorem (39, 40), the two particles on the bilayer and the cytoskeleton move together. This is indicated by the overlapped red solid and dashed lines in Fig. 3*B*. Hence, there is no significant bilayer–cytoskeletal slip in this case. However, assuming a pathological RBC state where f_{bs} is decreased by one or two orders of magnitude, an apparent bilayer–cytoskeletal slip occurs after a few TT cycles. Specifically, the TT frequency of the bilayer and the cytoskeleton with $f_{bs} = 0.194$ pN·μm^{-1}·s^{-1} is greater than the frequency of the cytoskeleton but lower than the frequency of the lipid bilayer in the case with $f_{bs} = 0.00194$ pN·μm^{-1}·s^{-1}. For comparison, two cases of the one-component DPD model are also shown in Fig. 3*B*: one with the local area modulus $k_l = 2\mu_S$ and the other with $k_l = 10^3\mu_S$. We find that the frequency of the latter case is close to the case of the two-component model with $f_{bs} = 0.194$ pN·μm^{-1}·s^{-1}. This is because there is no bilayer–cytoskeletal slip with large f_{bs} and the local area deformation of the cytoskeleton is the same as that of the bilayer; hence we have local conservation of the surface area of the cytoskeleton in agreement with ref. 41. The frequency of the one-component model with area modulus $k_l = 2\mu_s$ is even greater than the frequency of the bilayer in the case of two-component model $f_{bs} = 0.00194$ pN·μm^{-1}·s^{-1}, because it is close to
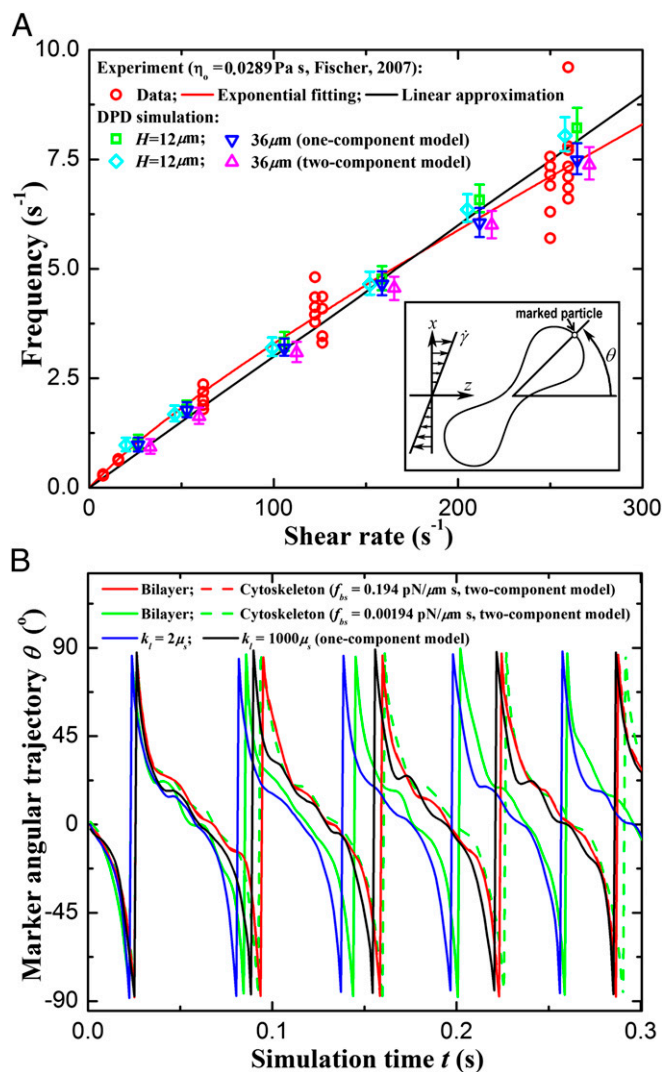
Fig. 3. Tank-treading motion of a RBC in shear flow. (*A*) TT frequency as a function of shear rate (the data of the two-component model are shifted horizontally for clarity; the error bars are obtained by increasing or decreasing membrane viscosities by 10% from their default values; η_0 is the suspending medium viscosity). Experimental data (red circles) from ref. 17 are shown. The TT frequency is investigated by tracking the marked particle in the RBC membrane. *Inset* shows the schematic diagram of the TT RBC in a shear flow. θ represents the angle between the position vector of the marked particle and flow direction. (*B*) Angular trajectory (θ) as a function of time. For the case with $f_{bs} = 0.194$ pN·μm^{-1}·s^{-1}, the bilayer and the cytoskeleton are represented by red solid and dashed lines, respectively. For the case with $f_{bs} = 0.00194$ pN·μm^{-1}·s^{-1}, they are represented by green solid and dashed lines, respectively. f_{bs} denotes the friction coefficient of the bilayer–cytoskeletal interaction. The one-component model cases with local area modulus $k_l = 2\mu_s$ and $k_l = 10^3\mu_s$ are represented by blue and black solid lines, respectively, where μ_s is the shear modulus.

the case of the two-component model with $f_{bs} = 0.0$. In this case we do not have local conservation of the surface area of the cytoskeleton in contrast to ref. 41 but in agreement with ref. 42. Hence, our two-component model can be used to quantify the existence of slip and the cytoskeletal local surface area preservation depending on the RBC state, e.g., in health or in diseases with reduced transmembrane protein density (40). In summary, we resolved two-decades-old controversies on the dependence of TT frequency on shear rate and the role of bilayer–cytoskeletal slip, with the resolution of the latter achieved only by explicitly incorporating the bilayer–cytoskeletal friction in the two-component model.
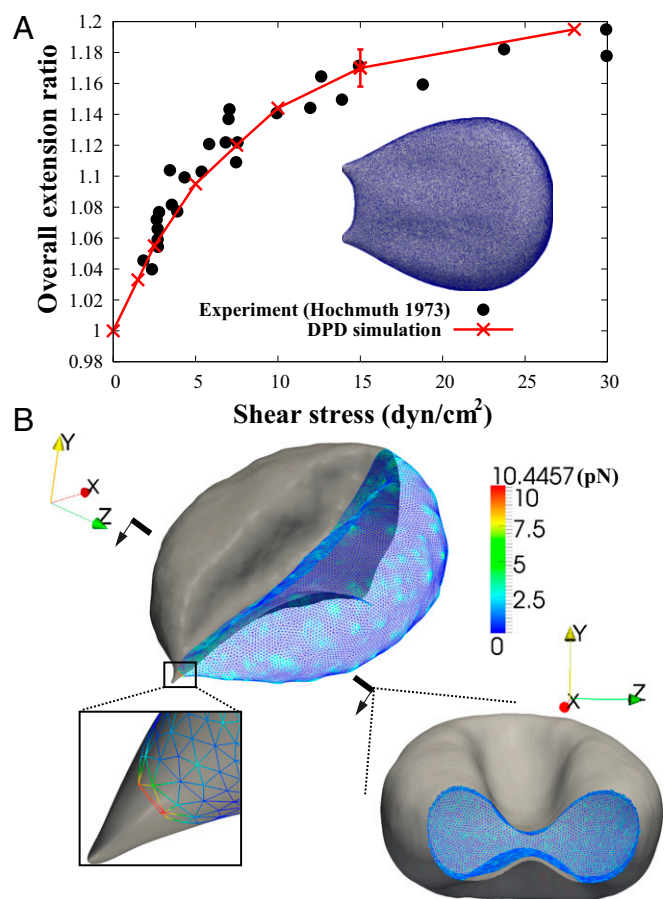
Bilayer–Cytoskeletal Detachment in Channel Flow. Another important and largely unresolved problem in RBC mechanics involves determining the forces needed to detach the lipid bilayer from the cytoskeleton (43). The prevalent description of this bilayer–cytoskeletal interaction strength is based on the definition of an adhesion energy W_0 (43, 44). Although this adhesion energy model matches well with experimental data, this description involving W_0 does not provide mechanistic insights into the molecular origin of the bilayer–cytoskeletal interaction. The assumption in the adhesion energy model that the bilayer–cytoskeletal adhesion is a continuum property of the membrane is not rigorously true, because integral proteins are known to create discrete attachments of the spectrin network to the lipid bilayer. Therefore, we use our two-component model with $N_v = 23{,}867$ to predict the bilayer–cytoskeletal interaction force explicitly and directly at the molecular level when the bilayer–cytoskeletal bonds rupture occurs under a certain threshold value of shear stress (~1.5 dyn/cm^2 or 0.15 pN/μm^2) during the tethering process in channel flow (18). The detailed simulation setup can be found in *SI Text*.

First, we model whole-cell stretching, with a line attachment between the cell and the substrate instead of a single-point attachment. The dependence predicted in the DPD simulation of the extension ratio of the RBC on the shear stress matches well with the experimental data shown in Fig. 4A. The extension ratio is defined as the ratio of maximum dimension between the current cell shape and the initial cell shape.

Next, we simulate the case with one attachment point. The bilayer–cytoskeletal interaction force applied on a single junctional complex in the case of critical shear stress (0.15 pN/μm^2) is shown in Fig. 4B, and the bilayer–cytoskeletal interaction strength, i.e., the maximum force applied on a junctional complex, is estimated as $\sigma_{bs} = 10.45$ pN. Hwang and Waugh (43) reported that the bilayer–cytoskeletal adhesion energy W_0 is about 60 μJ/m^2. Following the scenario that during dissociation band 3 is separated from the bilayer, this adhesion energy is related to the energy to pull band 3 out. Taking into account the fact that band 3 is a chain that crosses the bilayer 14 times (45), the subsequent adhesion energy is the energy required to pull all these crossings sequentially out. Assuming that during the process the applied force decreases linearly from the critical contact force to zero as band 3 is completely taken out, the adhesion energy is given as $W_0 = (5 \text{ nm} \times 14/2) \cdot \sigma_{bs}/A_{jc}$, for a bilayer thickness of 5 nm, where A_{jc} is the area of a junctional complex. If the junctional complex is assumed to be circular with a diameter of 75 nm and area is $A_{jc} = 0.004418$ μm^2, then $W = 80$ μJ / m^2, which is close to the value (60 μJ/m^2) obtained by Hwang and Waugh (43). In summary, these simulations lead to direct quantification of molecular-level mechanical forces involved in bilayer–cytoskeletal dissociation. Such quantitative assessment is essential for elucidating bilayer loss in RBC diseases such as hereditary spherocytosis (4) and sickle-cell anemia (1).

Conclusions. In this work, we have presented a unique computational framework for simulating the interactions between the lipid bilayer and the cytoskeletal network of human RBCs. This mesoscale analysis, predicated on dissipative particle dynamics, is tested and validated through rigorous comparisons with experimental data from four different sets of independent experiments that probe different aspects of biophysical and rheological properties of RBCs. Furthermore, the present two-component model is compared with corresponding results obtained from prior one-component model predictions and with theoretical estimates, wherever appropriate. The capabilities and limitations of the two-component model are assessed.

By applying the two-component whole-cell model, we also reconciled and resolved several controversies and issues in RBC mechanics. First, we were able to realistically model the micropipette aspiration experiments of measuring both the area moduli of

Fig. 4. Bilayer–cytoskeletal detachment in channel flow. (A) Comparison of cell extension ratio between the DPD simulation and the experiment for the whole-cell stretching with a line attachment (18). The error bars are obtained by increasing or decreasing the default value of shear modulus μ_s by 10%. (B) Simulation of the bilayer–cytoskeletal detachment in channel flow. *Inset* shows the local view of the bilayer–cytoskeletal interaction near the attachment point. The bilayer is shown as a gray surface and the cytoskeleton is shown as a triangular network with the contour. The contour is the magnitude of the bilayer–cytoskeletal interaction force on a junctional complex. The unit of force is pico-Newtons (pN).

the cytoskeleton (k_s) and the lipid bilayer (k_l), using the same set of input parameters, although these two area moduli differ by five orders of magnitude. Second, we found that the two-component model matches the thermal fluctuations experiments better than the one-component model due to the explicit incorporation of bilayer–cytoskeletal elastic interaction. Third, we found that the dependence of the tank-treading frequency on the shear rate follows a linear relationship for a narrow channel but a nonlinear one for a wide channel, hence reconciling a controversy in the literature (17). In addition, we demonstrated that the tank-treading motion is too fast for the bilayer–cytoskeletal slip to occur for healthy RBCs; however, we also showed that apparent bilayer–cytoskeletal slip occurs if the bilayer–cytoskeletal friction coefficient f_{bs} is significantly reduced for certain diseases. Finally, we quantified the strength of the force per junctional complex by which the bilayer remains attached to the cytoskeleton at the molecular level during RBC tethering in the channel flow experiment.

Methods

In this unique two-component RBC model, the membrane is modeled by two different components, i.e., the lipid bilayer and the cytoskeleton. Specifically, each component is constructed by a 2D triangulated network with N_v vertices, where each vertex is represented by a DPD particle as shown in

Fig. S1A. The potential of the RBC membrane including these two different components is written as

$$U = U_s + U_b + U_{a+v} + U_{int}, \qquad [1]$$

where U_s is the spectrin's potential energy from the cytoskeleton, U_b is the bending energy from the lipid bilayer, U_{a+v} corresponds to the area and volume conservation constraints from the lipid bilayer, and U_{int} is the potential energy of the interaction between the lipid bilayer and the cytoskeleton. The detailed expressions of U_s, U_b, and U_{a+v} can be found in *SI Text*.

The bilayer–cytoskeletal interaction potential U_{int} can be expressed as a summation of harmonic potentials given by

$$U_{int} = \sum_{j \in 1...N_{bs}} \frac{k_{bs}(d_j - d_{j0})^2}{2}. \qquad [2]$$

Here N_{bs} is the number of bond connections between the bilayer and the cytoskeleton, i.e., the interactions between the transmembrane proteins (band 3 and glycophorin C) and spectrins; k_{bs} denotes the spring constant of the bond; d_j is the distance between the vertex j of the cytoskeleton and the corresponding projection point j' on the lipid bilayer as shown in Fig. S1C; and d_{j0} is the initial distance between the vertex j and the point j'. The vertex in the spectrin cytoskeletal network is projected onto the closest triangle face of the lipid bilayer, and the distance and relative velocity between the cytoskeleton vertex and its projection point on the lipid bilayer

are obtained. The corresponding elastic force on the vertex j of the cytoskeleton is given as

$$\mathbf{f}_j^E = k_{bs}(d_j - d_{j0})\mathbf{n}_j, \qquad [3]$$

where $\mathbf{n}_j$ is the normal direction of the lipid-bilayer surface at the projection point of vertex j.

The tangential friction force between the lipid bilayer and the cytoskeleton on the vertex j of the cytoskeleton is given as

$$\mathbf{f}_j^F = -f_{bs}[\mathbf{v}_j - (\mathbf{v}_j \cdot \mathbf{n}_j)\mathbf{n}_j], \qquad [4]$$

where f_{bs} is the tangential friction coefficient, and $\mathbf{v}_j$ is the relative velocity between the vertex j and the corresponding projection point j' on the lipid bilayer. Detailed descriptions of other aspects of the model, e.g., membrane viscosities, can be found in *SI Text*.

1. Liu SC, Derick LH, Zhai S, Palek J (1991) Uncoupling of the spectrin-based skeleton from the lipid bilayer in sickled red cells. *Science* 252(5005):574–576.
2. Mohandas N, Evans EA (1994) Mechanical properties of the red cell membrane in relation to molecular structure and genetic defects. *Annu Rev Biophys Biomol Struct* 23:787–818.
3. Suresh S, et al. (2005) Connections between single-cell biomechanics and human disease states: Gastrointestinal cancer and malaria. *Acta Biomater* 1(1):15–30.
4. Walensky L, Mohandas N, Lux SE (2003) Disorders of the red blood cell membrane. *Blood, Principles and Practice of Hematology*, eds Handin RI, Lux SE, Stossel TP (Lippincott Williams & Wilkins, Philadelphia), 2nd Ed, pp 1709–1858.
5. Safeukui I, et al. (2012) Quantitative assessment of sensing and sequestration of spherocytic erythrocytes by the human spleen. *Blood* 120(2):424–430.
6. Deplaine G, et al. (2011) The sensing of poorly deformable red blood cells by the human spleen can be mimicked in vitro. *Blood* 117(8):e88–e95.
7. Li XJ, Vlahovska PM, Karniadakis GE (2013) Continuum- and particle-based modeling of shapes and dynamics of red blood cells in health and disease. *Soft Matter* 9(1):28–37.
8. Discher DE, Boal DH, Boey SK (1998) Simulations of the erythrocyte cytoskeleton at large deformation. II. Micropipette aspiration. *Biophys J* 75(3):1584–1597.
9. Li J, Dao M, Lim CT, Suresh S (2005) Spectrin-level modeling of the cytoskeleton and optical tweezers stretching of the erythrocyte. *Biophys J* 88(5):3707–3719.
10. Li J, Lykotrafitis G, Dao M, Suresh S (2007) Cytoskeletal dynamics of human erythrocyte. *Proc Natl Acad Sci USA* 104(12):4937–4942.
11. Li H, Lykotrafitis G (2012) Two-component coarse-grained molecular-dynamics model for the human erythrocyte membrane. *Biophys J* 102(1):75–84.
12. Discher DE, Mohandas N, Evans EA (1994) Molecular maps of red cell deformation: Hidden elasticity and in situ connectivity. *Science* 266(5187):1032–1035.
13. Knowles DW, Tilley L, Mohandas N, Chasis JA (1997) Erythrocyte membrane vesiculation: Model for the molecular mechanism of protein sorting. *Proc Natl Acad Sci USA* 94(24):12969–12974.
14. Park Y, et al. (2008) Refractive index maps and membrane dynamics of human red blood cells parasitized by *Plasmodium falciparum*. *Proc Natl Acad Sci USA* 105(37):13730–13735.
15. Park Y, et al. (2010) Measurement of red blood cell mechanics during morphological changes. *Proc Natl Acad Sci USA* 107(15):6731–6736.
16. Byun HS, et al. (2012) Optical measurement of biomechanical properties of individual erythrocytes from a sickle cell patient. *Acta Biomater* 8(11):4130–4138.
17. Fischer TM (2007) Tank-tread frequency of the red cell membrane: Dependence on the viscosity of the suspending medium. *Biophys J* 93(7):2553–2561.
18. Hochmuth RM, Mohandas N, Blackshear PL, Jr. (1973) Measurement of the elastic modulus for red cell membrane using a fluid mechanical technique. *Biophys J* 13(8):747–762.
19. Fedosov DA, Caswell B, Karniadakis GE (2010) A multiscale red blood cell model with accurate mechanics, rheology, and dynamics. *Biophys J* 98(10):2215–2225.
20. Reasor DA, Clausen JR, Aidun CK (2011) Coupling the lattice-Boltzmann and spectrin-link methods for the direct numerical simulation of cellular blood flow. *Int J Numer Methods Fluids* 68:767–781.
21. Noguchi H, Gompper G (2005) Shape transitions of fluid vesicles and red blood cells in capillary flows. *Proc Natl Acad Sci USA* 102(40):14159–14164.
22. Evans EA, Waugh R, Melnik L (1976) Elastic area compressibility modulus of red cell membrane. *Biophys J* 16(6):585–595.
23. Waugh R, Evans EA (1979) Thermoelasticity of red blood cell membrane. *Biophys J* 26(1):115–131.

24. Peng Z, Asaro RJ, Zhu Q (2010) Multiscale simulation of erythrocyte membranes. *Phys Rev E Stat Nonlin Soft Matter Phys* 81(3 Pt 1):031904.
25. Pivkin IV, Karniadakis GE (2008) Accurate coarse-grained modeling of red blood cells. *Phys Rev Lett* 101(11):118105.
26. Brochard F, Lennon JF (1975) Frequency spectrum of the flicker phenomenon in erythrocytes. *J Phys* 36:1035–1047.
27. Strey H, Peterson M, Sackmann E (1995) Measurement of erythrocyte membrane elasticity by flicker eigenmode decomposition. *Biophys J* 69(2):478–488.
28. Gov NS, Zilman AG, Safran SA (2003) Cytoskeleton confinement and tension of red blood cell membranes. *Phys Rev Lett* 90(22):228101.
29. Dubus C, Fournier JB (2006) A Gaussian model for the membrane of red blood cells with cytoskeletal defects. *Europhys Lett* 75(1):181–187.
30. Zhang R, Brown FL (2008) Cytoskeleton mediated effective elastic properties of model red blood cell membranes. *J Chem Phys* 129(6):065101.
31. Rochal SB, Lorman VL (2006) Cytoskeleton influence on normal and tangent fluctuation modes in the red blood cells. *Phys Rev Lett* 96(24):248102.
32. Fedosov DA, Lei H, Caswell B, Suresh S, Karniadakis GE (2011) Multiscale modeling of red blood cell mechanics and blood flow in malaria. *PLOS Comput Biol* 7(12):e1002270.
33. Auth T, Safran SA, Gov NS (2007) Fluctuations of coupled fluid and solid membranes with application to red blood cells. *Phys Rev E Stat Nonlin Soft Matter Phys* 76(5 Pt 1):051910.
34. Milner ST, Safran SA (1987) Dynamical fluctuations of droplet microemulsions and vesicles. *Phys Rev A* 36(9):4371–4379.
35. Fischer TM, Stöhr-Lissen M, Schmid-Schönbein H (1978) The red cell as a fluid droplet: Tank tread-like motion of the human erythrocyte membrane in shear flow. *Science* 202(4370):894–896.
36. Tran-Son-Tay R, Sutera SP, Rao PR (1984) Determination of red blood cell membrane viscosity from rheoscopic observations of tank-treading motion. *Biophys J* 46(1):65–72.
37. Perrotta S, et al. (2005) The N-terminal 11 amino acids of human erythrocyte band 3 are critical for aldolase binding and protein phosphorylation: Implications for band 3 function. *Blood* 106(13):4359–4366.
38. Oishi M, Utsubo K, Kinoshita H, Fujii T, Oshima M (2012) Continuous and simultaneous measurement of the tank-treading motion of red blood cells and the surrounding flow using translational confocal micro-particle image velocimetry (micro-PIV) with sub-micron resolution. *Meas Sci Technol* 23(3):035301.
39. Peng Z, Asaro R, Zhu Q (2011) Multiscale modeling of erythrocytes in Stokes flow. *J Fluid Mech* 686:299–337.
40. Peng Z, Zhu Q (2013) Deformation of the erythrocyte cytoskeleton in tank treading motions. *Soft Matter* 9(31):7617–7627.
41. Fischer TM (1992) Is the surface area of the red cell membrane skeleton locally conserved? *Biophys J* 61(2):298–305.
42. Dodson WR, 3rd, Dimitrakopoulos P (2010) Tank-treading of erythrocytes in strong shear flows via a nonstiff cytoskeleton-based continuum computational modeling. *Biophys J* 99(9):2906–2916.
43. Hwang WC, Waugh RE (1997) Energy of dissociation of lipid bilayer from the membrane skeleton of red blood cells. *Biophys J* 72(6):2669–2678.
44. Hochmuth RM, Marcus WD (2002) Membrane tethers formed from blood cells with available area and determination of their adhesion energy. *Biophys J* 82(6):2964–2969.
45. Lux SE, John KM, Kopito RR, Lodish HF (1989) Cloning and characterization of band 3, the human erythrocyte anion-exchange protein (AE1). *Proc Natl Acad Sci USA* 86(23):9089–9093.

BIOPHYSICS AND COMPUTATIONAL BIOLOGY

ENGINEERING

Supporting Information

Peng et al. 10.1073/pnas.1311827110

SI Text

Methods and Models

First, we briefly describe the dissipative particle dynamics (DPD) method. Second, we present details of the two-component red blood cell (RBC) model, including the elasticity of both the lipid bilayer and the cytoskeleton, the bilayer–cytoskeletal interactions, and membrane viscosities. Third, we derive the scaling relationships between model units and physical units.

Dissipative Particle Dynamics. The DPD method is a particle-based mesoscopic simulation technique that allows modeling of fluids and soft matter. A DPD system is represented by N particles, which interact through pairwise effective potentials and move according to Newton's second law (1, 2). In a DPD simulation, a particle represents the center of mass in a cluster of atoms, and the position and momentum of the particle are updated in a continuous phase but spaced at discrete time steps. Particles i and j at positions r_i and r_j interact with each other via pairwise conservative, dissipative, and random forces, which are given by

$$F_{ij}^C = a_{ij}\omega(r_{ij})\mathbf{n}_{ij}, \qquad [S1]$$

$$F_{ij}^D = -\gamma\omega^2(r_{ij})(\mathbf{n}_{ij}\cdot\mathbf{v}_{ij})\mathbf{n}_{ij}, \qquad [S2]$$

$$F_{ij}^R = \sigma\omega(r_{ij})\zeta_{ij}\Delta t^{-1/2}\mathbf{n}_{ij}, \qquad [S3]$$

where $\mathbf{r}_{ij} = \mathbf{r}_i - \mathbf{r}_j$, $r_{ij} = |\mathbf{r}_{ij}|$, $\mathbf{n}_{ij} = \mathbf{r}_{ij}/r_{ij}$, and $\mathbf{v}_{ij} = \mathbf{v}_i - \mathbf{v}_j$. The coefficients a_{ij}, γ, and σ define, respectively, the strength of conservative, dissipative, and random forces. In addition, ζ_{ij} is a random number with zero mean and unit variance, and Δt is the time-step size. The weight function $\omega(r_{ij})$ is given by

$$\omega(r_{ij}) = \begin{cases} 1 - r_{ij}/r_c & r_{ij} < r_c \\ 0 & r_{ij} \geq r_c, \end{cases} \qquad [S4]$$

where r_c is the cutoff radius, which gives the extent of the interaction range. In the DPD method, the dissipative force and the random force act as heat sink and source, respectively, and the combined effect of the two forces acts a thermostat. Also, a common choice of the soft repulsion for the conservative force permits us to use larger integration time steps than are usually allowed by the molecular dynamics (MD) simulation technique; thus, DPD is a simple but efficient simulation method that correctly represents hydrodynamic interactions.

Membrane Elasticity of the Two-Component RBC Model. In this unique two-component RBC model, the membrane is modeled by two different components, i.e., the lipid bilayer and the cytoskeleton, as shown in Fig. S1A. Specifically, each component is constructed by a 2D triangulated network with N_v vertices, where each vertex is represented by a DPD particle. Different from the one-component DPD model, the lipid bilayer has no shear stiffness but only bending stiffness and a very large local area stiffness, whereas the inner layer (cytoskeleton) has no bending stiffness but a large shear stiffness. The potential of the RBC membrane including these two different components is written as

$$U = U_s + U_b + U_{a+v} + U_{int}, \qquad [S5]$$

where U_s is the spring's potential energy from the cytoskeleton, given by

$$U_s = \sum_{j\in 1\ldots N_s}\left[\frac{k_B T l_m\left(3x_j^2 - 2x_j^3\right)}{4p\left(1 - x_j\right)} + \frac{k_p}{(n-1)l_j^{n-1}}\right], \qquad [S6]$$

where N_s is the number of springs, l_j is the length of the spring j, l_m is the contour length, $x_j = l_j/l_m$, p is the persistence length, k_B is the Boltzmann constant, T is the temperature, k_p is the spring constant, and n is a parameter. The first term is a worm-like chain (WLC) model (3) and the second term is a repulsive force term. Note that in the finite-element simulation (4), instead of using this exponential form of repulsive force, a simple functional form C/A is used, where C is a constant and A is the area of the corresponding triangle in the spectrin network. To be consistent in the comparison with the finite-element method (FEM) simulation result, we also used the same function form C/A in the prestressed DPD simulation case of micropipette aspiration. The isotropic mean stress for an equilateral triangle in the network is given as

$$\overline{T} = -\frac{3lf_{WLC}(l)}{4A} - \frac{C}{A^2}, \qquad [S7]$$

where l is the length of the spectrin link, $f_{WLC}(l)$ is the force of the WLC model, and $A = \sqrt{3}l^2/4$.

In our simulations, we have $\overline{T} = 0$ for the lipid bilayer. For the cytoskeleton, we also have $\overline{T} = 0$ in the case of stress-free initial configuration, but in the case of prestressed initial configuration, $\overline{T}$ can be nonzero; e.g., $\overline{T} = -30$ pN/μm.

Also, U_b is the bending energy from the lipid bilayer, given by

$$U_b = \sum_{j\in 1\ldots N_s} k_b\left[1 - \cos\left(\theta_j - \theta_0\right)\right], \qquad [S8]$$

where k_b is the bending coefficient and $k_b = 2k_c/\sqrt{3}$, where k_c is the bending stiffness of the bilayer. Also, θ_j is the instantaneous angle between two adjacent triangles as shown in Fig. S1B, and θ_0 is the spontaneous angle, which is set to zero in our simulations. Finally, U_{a+v} corresponds to the area and volume conservation constraints from the lipid bilayer, given by

$$U_{a+v} = \sum_{j\in 1\ldots N_t}\frac{k_l\left(A_j - A_0\right)^2}{2A_0} + \frac{k_v\left(V^{tot} - V_0^{tot}\right)^2}{2V_0^{tot}}, \qquad [S9]$$

where N_t is the number of triangles in the lipid bilayer, A_j is the instantaneous triangle area as shown in Fig. S1B, and A_0 is the initial triangle area. V^{tot} is the current total RBC volume, and V_0^{tot} is the initial total RBC volume. Also, k_l and k_v are the bilayer local area constraint coefficient and the global volume constraint coefficient, respectively.

Bilayer–Cytoskeletal Interactions. In addition to the commonly used elastic potentials for the membrane, we invoke another term U_{int} to capture the interaction between the lipid bilayer and the cytoskeleton, which can be expressed as a summation of harmonic potentials given by

$$U_{int} = \sum_{j\in 1\ldots N_{bs}}\frac{k_{bs}\left(d_j - d_{j0}\right)^2}{2}. \qquad [S10]$$

Here N_{bs} is the number of bond connections between the bilayer and the cytoskeleton, i.e., the interactions between the transmembrane proteins (band 3 and glycophorin C) and spectrins, which is set to be the same as the number of vertices N_v in the current model; k_{bs} denotes the spring constant of the bond. Although there are two kinds of interactions in each junctional complex, including the major connections via band 3 and ankyrin and the secondary connections via actin, glycophorin C, and band 4.1, here we consider them together as an effective bilayer–cytoskeletal interaction in one junctional complex and model this interaction as a normal viscoelastic spring along with a tangential friction force as shown in Fig. S1 C and D. As shown in Fig. S1C, d_j is the distance between the vertex j of the cytoskeleton and the corresponding projection point j' on the lipid bilayer; and d_{j0} is the initial distance between the vertex j and the point j', which is set to zero in our simulations. Experiments show that $d_{j0} \approx 30$ nm (5), but we found that the difference is negligible in our simulations. Also, $\mathbf{n}_j$ is the normal direction of the lipid-bilayer surface at the projection point of vertex j. Numerically, a master–slave penalty contact algorithm is applied to calculate the force (6). The vertex in the spectrin cytoskeletal network is projected onto the closest triangle face of the lipid bilayer, and the distance and relative velocity between the cytoskeleton vertex and its projection point on the lipid bilayer are obtained as shown in Fig. S1C.

The corresponding elastic force on the vertex j of the cytoskeleton is given as

$$\mathbf{f}_j^E = k_{bs}(d_j - d_{j0})\mathbf{n}_j, \qquad \text{[S11]}$$

and the vertical damping force related to this elastic spring is

$$\mathbf{f}_j^D = -c_{bs}(\mathbf{v}_j \cdot \mathbf{n}_j)\mathbf{n}_j, \qquad \text{[S12]}$$

where c_{bs} is the vertical damping coefficient, and $\mathbf{v}_j$ is the relative velocity between the vertex j and the corresponding projection point j' on the lipid bilayer. The tangential friction force between the lipid bilayer and the cytoskeleton is given as

$$\mathbf{f}_j^F = -f_{bs}[\mathbf{v}_j - (\mathbf{v}_j \cdot \mathbf{n}_j)\mathbf{n}_j], \qquad \text{[S13]}$$

where f_{bs} is the tangential friction coefficient.

To ensure that the temperature is constant, another random force term is added, as in ref. 7,

$$\mathbf{f}_j^R \Delta t = \sqrt{2k_B T}\left(\sqrt{2f_{bs}}d\mathbf{W}_{ij}^A + \sqrt{3c_{bs}}\frac{tr[d\mathbf{W}_{ij}]}{3}\mathbf{1}\right)\cdot\mathbf{n}_j, \qquad \text{[S14]}$$

where $tr[d\mathbf{W}_{ij}]$ is the trace of a random matrix of independent Wiener increments of $d\mathbf{W}_{ij}$. The Wiener increment $d\mathbf{W}_{ij}(t) = \mathbf{W}_{ij}(t+\Delta t) - \mathbf{W}_{ij}(t)$ over a time-step Δt is a random variable drawn from a normal distribution with zero mean and a time-step variance $\mathcal{N}[0, \Delta t]$. $d\mathbf{W}_{ij}^A = (d\mathbf{W}_{ij} - d\mathbf{W}_{ji})/2$ is the antisymmetric part, and Δt is the magnitude of the time step.

Hence, the total interaction force is given by

$$\mathbf{f}_j^{int} = \mathbf{f}_j^E + \mathbf{f}_j^D + \mathbf{f}_j^F + \mathbf{f}_j^R. \qquad \text{[S15]}$$

In addition, $\mathbf{f}_j^{int}$ is also distributed to the three vertices of the corresponding bilayer triangle with one-third of the magnitude and an opposite sign to follow Newton's third law. For simplicity, the vertical damping coefficient is always set to be the same as the friction coefficient; i.e., $c_{bs} = f_{bs}$.

Membrane Viscosities. The membrane viscosity is incorporated into both the lipid bilayer and the cytoskeleton by adding two terms, i.e., dissipative and random forces, respectively, as

$$\mathbf{F}_{ij}^{D,k} = -\gamma_k^T \mathbf{v}_{ij} - \gamma_k^C(\mathbf{v}_{ij} \cdot \mathbf{e}_{ij})\mathbf{e}_{ij}, \qquad \text{[S16]}$$

$$\mathbf{F}_{ij}^{R,k}\Delta t = \sqrt{2k_B T}\left(\sqrt{2\gamma_k^T}d\overline{\mathbf{W}_{ij}^S} + \sqrt{3\gamma_k^C - \gamma_k^T}\frac{tr[d\mathbf{W}_{ij}]}{3}\mathbf{1}\right)\cdot\mathbf{e}_{ij}, \quad \text{[S17]}$$

where γ_k^T and γ_k^C are dissipative parameters $(3\gamma_k^C > \gamma_k^T)$; and $\mathbf{e}_{ij}$ and $\mathbf{v}_{ij}$ are the relative position and velocity vectors of spring ends i and j. Also, $d\overline{\mathbf{W}_{ij}^S} = d\mathbf{W}_{ij}^S - tr[d\mathbf{W}_{ij}^S]1/3$ is the traceless symmetric part of the random matrix of independent Wiener increments of $d\mathbf{W}_{ij}$, and $k = b, s$ stands for the lipid bilayer or the cytoskeleton, respectively. The viscosities of the lipid bilayer and the cytoskeleton can be calculated as

$$\eta_k = \sqrt{3}\gamma_k^T + \frac{\sqrt{3}\gamma_k^C}{4}. \qquad \text{[S18]}$$

Experiments show that the cytoskeleton viscosity η_s is about 50–100 times larger than the lipid-bilayer viscosity η_b (8).

Scaling of DPD Model and Physical Units. Within the DPD approach, reduced units are used for the mass, length, and energy. In the following, we derive the scaling relationships between model units and physical units.

Let $r = 1$ m denote the length scale in the physical system in SI units and r' denote the length scale of the DPD model. The same initial diameter ($D_0 = 7.82$ μm) of the RBC can be expressed in both the DPD system and the physical system as

$$D_0 = D_0^M \cdot r' = D_0^P \cdot r = 7.82 \times 10^{-6}\,\text{m}, \qquad \text{[S19]}$$

where $D_0^P = 7.82 \times 10^{-6}$ and m is meter. The variables with upper index "P" (e.g., D_0^P) are values (numbers without units) of the quantities (e.g., D_0) in the physical system with SI units, whereas the variables with upper index "M" (e.g., D_0^M) are values (numbers without units) of the quantities (e.g., D_0) in the DPD system. We can choose the length-scale r' of the DPD system, and usually specific values of r' and D_0^M depend on the size of the DPD system.

Because

$$\left[\frac{k_B T}{\mu_s}\right] = \text{length}^2, \qquad \text{[S20]}$$

where $[\cdot]$ denotes the dimension of a quantity, μ_s is the shear modulus, k_B is the Boltzmann constant, and T is the temperature, we should have

$$\frac{k_B T}{\mu_s} = \frac{(k_B T)^M}{\mu_s^M}(r')^2 = \frac{(k_B T)^P}{\mu_s^P}(r)^2. \qquad \text{[S21]}$$

Plugging Eq. S19 into Eq. S21, we get

$$(k_B T)^M = \frac{\mu_s^M}{\mu_s^P}\left(\frac{D_0^M}{D_0^P}\right)^2 (k_B T)^P. \qquad \text{[S22]}$$

Similarly for the force N, because

$$\left[\frac{k_B T}{N}\right] = \text{length}, \qquad \text{[S23]}$$

we have

$$N^M = \frac{(k_B T)^M}{(k_B T)^P}\frac{r^M}{r^P}N^P = \frac{(k_B T)^M}{(k_B T)^P}\frac{D_0^P}{D_0^M}N^P = \frac{\mu_s^M}{\mu_s^P}\frac{D_0^M}{D_0^P}N^P. \qquad \text{[S24]}$$

For time scaling, because

$$\left[\frac{\eta D_0^2}{N}\right] = \text{time},$$ [S25]

where η is a characteristic viscosity, we have

$$\frac{\eta D_0^2}{N} = \frac{\eta^M \left(D_0^M\right)^2}{N^M}\tau' = \frac{\eta^P \left(D_0^P\right)^2}{N^P}\tau,$$ [S26]

where $\tau = 1$ s is the timescale in the physical system with SI units, and τ' is the timescale in the DPD system. Plugging Eq. **S24** into Eq. **S26**, we get the timescale of the DPD system as

$$\tau' = \frac{D_0^P}{D_0^M}\frac{\eta^P}{\eta^M}\frac{\mu_s^M}{\mu_s^P}\ \text{s},$$ [S27]

where s denotes second.

For example, in the simulations of tank-treading motions, the RBC diameter, the membrane Young's modulus, and the interior fluid viscosity are $D_0^M = 7.82$, $\mu_s^M = 12.125$, and $\eta^M = 1.8$, respectively, corresponding to $D_0^P = 7.82 \times 10^{-6}$, $\mu_s^P = 4.725 \times 10^{-6}$, and $\eta^P = 0.006$ in the physical system with SI units. Hence, the DPD timescale is $\tau' \simeq 2.7$ ms. In the simulations of tank-treading motions, a time-step size $\Delta t^M = (0.0005 \sim 0.005)$ in DPD units is used, which gives $\Delta t = \Delta t^M \tau' = (1.35 \sim 13.5)$ μs.

Comparison with Existing Models. Two-component whole-cell erythrocyte membrane models have been developed before (4, 9, 10). Compared with the existing models, the current two-component DPD model has three major advantages. The first advantage is that we explicitly model the bilayer–cytoskeletal interaction including the normal interaction and tangential friction based on realistic protein connectivity, in such a way that the bilayer–cytoskeletal interaction force and cytoskeleton deformation at the molecular level can be investigated directly. Second, we use a systematic coarse-graining procedure starting from the spectrin level (11, 12) so that different coarse-graining levels can be used to produce adequate levels of desired accuracy. Third, the model proposed here can predict the physical phenomena of quasi-static deformation, fluid dynamics, and thermal fluctuations, whereas some of the prior two-component whole-cell models (4, 10) cannot simulate thermal fluctuations. In addition, in contrast to the existing particle-based two-component model (9), our thermal fluctuation simulations have been validated extensively by comparing the results with experimental data (13).

In addition to two-component whole-cell models, there are also sophisticated two-component models of local membranes, in which only a small piece of RBC membrane is simulated, such as the model by Li and Lykotrafitis (14). Their model is more detailed with molecular information on lipid diffusion. Consequently, the computational cost is prohibitively high for it to be applicable to study whole-cell problems at the present time. However, the computational framework we present here can be further extended in future work to include these extra details as studied in ref. 14. As the first step, and for computational expediency, we neglect these details here and focus on the problems of the whole cell, such as in rheology, where details like lipid diffusion are not important. Hence, our two-component model is a good compromise between the one-component whole-cell DPD model and the two-component detailed molecular dynamics model in ref. 14. It can be used to explore important problems involving cell physiology and pathological states mediated by protein mutations, such as the bilayer loss in hereditary spherocytosis and the bilayer–cytoskeleton uncoupling in sickle-cell anemia (15).

Simulation Setups and Parameter Estimation

Here, we present details of the simulation setups of micropipette aspiration, membrane fluctuations, tank-treading motion, and channel flow stretching. Subsequently, we estimate the default main parameters.

Micropipette Aspiration Simulation Setup. In the micropipette aspiration (16), a negative pressure is applied to aspirate a RBC into a small glass pipette. The RBC membrane undergoes large deformation during this aspiration process. To measure the area deformation of the cytoskeleton alone, the actins in the RBC membrane are labeled using rhodamine–phalloidin, an antibody with fluorescence. By measuring the fluorescence light intensity, the actin density in different regions of the cytoskeleton can be determined, which is inversely proportional to the area deformation of the cytoskeleton. It was found that the cytoskeleton in the cap region of the aspirated cell inside the pipette is significantly expanded, whereas the cytoskeleton near the pipette entrance is compressed. The density of the lipid molecule marked by another antibody was found uniform over the cell surface because the lipid bilayer is incompressible. This experiment takes up to 30 min to allow the bilayer–cytoskeletal slip to reach steady state, so that it is modeled as a quasi-static process in our simulation; i.e., the bilayer–cytoskeletal friction and membrane viscosities are neglected. The parameters used in this simulation are listed in Table S1.

The RBCs are hypotonically swollen (osmotic pressure is in a typical range of 160–250 mOsm) in the beginning of this experiment (16) and correspondingly our RBC model is also inflated from a standard biconcave shape accordingly in the beginning of the simulation. A rigid cylindrical surface is used to represent the pipette. The interaction between the lipid bilayer and the pipette is modeled as a hard contact by using a master–slave algorithm (6) similar to the bilayer–cytoskeletal interaction but with a large spring constant. As indicated in the experiments, during the aspiration the membrane is usually separated from the pipette by a small gap of fluid so that the friction between them is insignificant and thus not considered in our model. We further simplify the fluid pressure distribution inside the pipette as a uniform pressure difference applied on the cap region of the lipid bilayer and a linear distribution along the aspiration length; the pressure difference equals zero at the entrance.

In addition to the results shown in Fig. 1 in the main text, we also applied the one-component DPD model to study this problem, and we found that the area expansion is abnormally large in the cap region. The reason is that we applied a uniform pressure on the cap region of the cell with a linear distribution along the aspiration length, which is different from the interaction pressure applied on the cytoskeleton from the lipid bilayer in the two-component model. Basically, the large local area modulus of the bilayer is absent in the one-component DPD model. In the Monte Carlo simulation (3), instead of applying the pressure to deform the cell, a canonical shape (cylinder/sphere) was assumed; the vertices of the triangular network were allowed to slide along this assumed shape.

Membrane Fluctuations Simulation Setup. We use the two-component DPD model to simulate membrane fluctuations. Because cells adhere to the substrate in the experiment, we fixed 13% of vertices on the RBC bottom and the simulations show that the effect of attachment strength (percentage of fixed vertices on the RBC bottom) on the amplitude fluctuations is negligible as long as more than 13% of the vertices are fixed (13). The extracellular and intracellular fluids with different viscosities were modeled using DPD particles. The top surface with a radius of 3 μm was monitored.

We did not use the full resolution model to study this problem because of computational cost. To reach the same timescale, the full resolution model with $N_v = 23,867$ is about 8,000 times more

expensive than the model with $N_v = 500$. The latter takes 1 h to run a typical case on a 32-core 800-MHz node.

Although we invoke a systematic coarse-graining approach (11, 12) for the in-plane mechanical properties such as shear modulus in the current study, the proper coarse-graining procedure for the properties of the bilayer–cytoskeletal interaction in the vertical direction in thermal fluctuations is unclear. For example, if we assume $k_{bs} = k_{bs}^{23,867}$ in the full resolution model with $N_v = 23,867$ and $k_{bs} = k_{bs}^{500}$ in the coarse-grained model with $N_v = 500$, it can be derived that $k_{bs}^{500} = 23,867/500 \cdot k_{bs}^{23,867} \approx 48 \cdot k_{bs}^{23,867}$, because $k_{bs}^{23,867}$ represents the stiffness of one junctional complex connection whereas k_{bs}^{500} represents the stiffness of 48 junctional complex connections. However, simulation results show this simple coarse-graining procedure makes the 500 DPD particle model too stiff in membrane fluctuation simulations. Lumping of 48 junctional complexes into one connection means that these junctional complexes always move with the same displacement, but in reality or in the simulation using the full resolution model with $N_v = 23,867$, the fluctuations of these 48 junctional complexes follow a distribution and their motions are not synchronized. Instead, simulations show that more reasonable results can be obtained by using $k_{bs}^{500} \approx k_{bs}^{23,867}$. Therefore, in the simulations of membrane fluctuations, we use the same physical values of k_{bs}, c_{bs}, and f_{bs} for different coarse-graining levels. For other simulations such as micropipette aspiration and tank-treading motion, we found the effect of k_{bs} is insignificant. The parameters used in this simulation are listed in Table S1.

Tank-Treading Simulation Setup. In the simulations of the tank-treading (TT) motion of a RBC in shear flow, we place a single RBC in linear shear flow between two planar solid walls and simulate the TT motion at different shear rates, using both the one-component and the two-component RBC models. The no-slip boundary condition between the fluid and the solid wall and that between the fluid and the RBC membrane are enforced using the bounce-back condition (17). The viscosity of the suspending medium is specified as $\eta_0 = 0.0289$ Pa s based on the experiment (18) and the viscosity of the cytosol inside the RBC is given as $\eta_1 = 0.006$ Pa s (19). For the membrane viscosities, it was found that the viscosity of the cytoskeleton is about 50 times larger than that of the lipid bilayer (8). By selecting the bilayer and cytoskeleton viscosities as $\eta_b = 0.008$ Pa s and $\eta_s = 0.372$ Pa s, respectively, the TT frequency matches the experimental results well as shown in Fig. 3A in the main text. Other parameters used in this simulation are listed in Table S1.

Channel Flow Stretching Simulation Setup. Channel flow stretching experiments have been carried out to examine the response of cells attached to a substrate to shear stresses exerted by an incoming flow. In a typical channel flow setup, erythrocytes are allowed to sediment inside a channel consisting of two parallel plates. The substrate is coated with BSA so that most cells do not adhere to the bottom plate with large attachment areas. When external flow is introduced, the cells deform while one point (in some cases more than one) remains attached to the substrate. Long membrane strands (tethers) may appear when the hydrodynamic shear exceeds a certain threshold value (~ 1.5 dyn/cm^2 or 0.15 pN/μm^2) (20).

In the simulation of whole-cell stretching with a line attachment between the cell and the substrate, two points at the bottom of the cell are fixed as shown in Fig. 4A, to create a line attachment. Because the line attachment edge of the cell was between 2 μm and 3 μm in the experiment, the distance between these two points is chosen with an average value of 2.5 μm in our simulations.

In the case with one attachment point, the cell attaches to the substrate not at a geometric point but within a small attachment area. In our model this attachment area is depicted as a circular area on the cell membrane whose diameter D_a is chosen to be

0.15 μm, which is within the same range as the diameter of the tether estimated from optical and scanning electron photomicrographs, i.e., 0.1–0.2 μm (20). It is important to note here that the two are not expected to be exactly the same, because the radius of the tether R_t depends on the applied force f_0 by the relation $R_t = 2\pi k_c/f_0$, where k_c is the bending stiffness (21).

Parameter Estimation. The default values of the main parameters of the two-component DPD model are listed in Table S1 for different cases. The initial membrane shear modulus without deformation μ_s is measured as 6 pN/μm in the micropipette aspiration experiment (19), but at a smaller value in the thermal fluctuations experiment (22). The shear modulus increases with deformation due to strain-induced stiffening (3) and may decrease at very large deformation due to spectrin unfolding (23). It can be one order higher for malaria-infected RBCs (24, 25). The bending modulus $k_c = 2.4 \times 10^{-19}$ J is a relatively well-accepted value (19). The membrane viscosity is measured as about 1.0 Pa s (26, 27), which is considered the sum of the bilayer viscosity η_b and the cytoskeleton viscosity η_s. According to Berk et al. (8), the cytoskeleton viscosity is 50–100 times larger than that of the bilayer viscosity. The membrane viscosity plays a significant role in tank-treading frequency (17) and by comparing predicted tank-treading frequency with experimental data we estimated typical values of η_b and η_s as shown in Table S1 and use them as default values.

The strength of the bilayer–cytoskeletal interaction bond is estimated on the order of 10 pN on a junctional complex in the current study by simulating the channel flow stretching experiment. If we assume the bond displacement to be around 0.2 μm when the bond breaks, a rough estimation of k_{bs} can be obtained as $k_{bs} = 10$ pN/0.2 μm = 50 pN/μm for a junctional complex. We used a default value of $k_{bs} = 46$ pN/μm as shown in Table S1. In addition, if we assume the stiffness of the bilayer–cytoskeletal interaction bond is in the same order of the stiffness of a spectrin, the linearized stiffness of a spectrin modeled using the WLC model is given as $k_{bs} = 3k_BT/2pL_c = 4$ pN/μm with a persistence length of $P = 7.5$ nm and contour length $L_c = 200$ nm (3); this can be considered as a lower-bound value. The bilayer–cytoskeletal friction coefficient f_{bs} has been estimated as 0.194 pN·μm^{-1}·s^{-1} for a single junctional complex based on the experimentally measured diffusivity of transmembrane proteins and the fluctuation dissipation theorem (10). For simplicity, the vertical damping coefficient is always set to be the same as the friction coefficient; i.e., $c_{bs} = f_{bs}$.

In addition to these main parameters, other parameters are given as follows: bilayer local area constraint $k_l = 5,000$ and global volume constraint $k_v = 5,000$ (both in DPD units). They serve as penalty parameters and their influence is negligible as long as their values are high enough. In Eq. S7, $n = 2$, $k_p = 1.0$, and $l_m = 2.2x_0$, where x_0 is the initial length of the spring in the cytoskeleton. The biconcave shape is chosen to be the stress-free state of the cytoskeleton, and $\theta_0 = 0$ in Eq. S8; i.e., the spontaneous curvature is zero.

One objective of the current study was to probe the mechanical characteristics associated with the bilayer–cytoskeletal viscoelastic interactions, which cannot be measured directly by existing experiments, and to investigate the effects of these mechanical parameters on overall experimental results. For example, in the fluorescence-marked micropipette aspiration experiments, we validate our model by predicting local cytoskeletal spectrin deformation. It mainly depends on the constitutive law of the cytoskeleton. Because it is a quasi-static process, the result is independent of dissipative parameters such as f_{bs}, η_b, and η_s; the influence of k_{bs} is found to be small as well. In the membrane fluctuations experiment, the amplitude of the fluctuations is independent of viscous parameters f_{bs}, η_b, and η_s (28, 29), and consequently we mainly study the effect of k_{bs} and μ_s. In the experiments involving tank-treading motion in shear flow, we focus on the effects of dissipative parameters f_{bs}, η_b, and η_s, because they play a major

role in influencing the tank-treading frequency. As for bilayer–cytoskeletal detachment in the channel flow experiments, our objective was to estimate bilayer–cytoskeletal bond strength σ_{bs}. Because only one or two parameters in each simulation of these four experiments are relevant to the result, our approach provides a good protocol in validating the two-component model and in investigating the effects of these parameters in isolation, in a systematic and controlled manner.

1. Hoogerbrugge PJ, Koelman JM (1992) Simulating microscopic hydrodynamic phenomena with dissipative particle dynamics. *Europhys Lett* 19(3):155–160.
2. Groot RD, Warren PB (1997) Dissipative particle dynamics: Bridging the gap between atomistic and mesoscopic simulation. *J Chem Phys* 107:4423–4435.
3. Discher DE, Boal DH, Boey SK (1998) Simulations of the erythrocyte cytoskeleton at large deformation. II. Micropipette aspiration. *Biophys J* 75(3):1584–1597.
4. Peng Z, Asaro RJ, Zhu Q (2010) Multiscale simulation of erythrocyte membranes. *Phys Rev E Stat Nonlin Soft Matter Phys* 81(3 Pt 1):031904.
5. Heinrich V, Ritchie K, Mohandas N, Evans E (2001) Elastic thickness compressibilty of the red cell membrane. *Biophys J* 81(3):1452–1463.
6. Malone JG, Johnson NL (1994) A parallel finite element contact/impact algorithm for nonlinear explicit transient analysis: Part I-The search algorithm and contact mechanics. *Int J Numer Methods Eng* 37:559–590.
7. Español P (1998) Fluid particle model. *Phys Rev E Stat Phys Plasmas Fluids Relat Interdiscip Topics* 57:2930–2948.
8. Berk DA, Hochmuth RM, Waugh RE (1989) Viscoelastic properties and rheology. *Red Blood Cell Membranes*, eds Agre P, Parker JC (Marcel Dekker, New York), pp 445–446.
9. Noguchi H, Gompper G (2005) Shape transitions of fluid vesicles and red blood cells in capillary flows. *Proc Natl Acad Sci USA* 102(40):14159–14164.
10. Peng Z, Asaro R, Zhu Q (2011) Multiscale modeling of erythrocytes in Stokes flow. *J Fluid Mech* 686:299–337.
11. Pivkin IV, Karniadakis GE (2008) Accurate coarse-grained modeling of red blood cells. *Phys Rev Lett* 101(11):118105.
12. Fedosov DA, Caswell B, Karniadakis GE (2010) Systematic coarse-graining of spectrin-level red blood cell models. *Comput Methods Appl Mech Eng* 199:1937–1948.
13. Fedosov DA, Lei H, Caswell B, Suresh S, Karniadakis GE (2011) Multiscale modeling of red blood cell mechanics and blood flow in malaria. *PLoS Comput Biol* 7(12):e1002270.
14. Li H, Lykotrafitis G (2012) Two-component coarse-grained molecular-dynamics model for the human erythrocyte membrane. *Biophys J* 102(1):75–84.
15. Liu SC, Derick LH, Zhai S, Palek J (1991) Uncoupling of the spectrin-based skeleton from the lipid bilayer in sickled red cells. *Science* 252(5005):574–576.
16. Discher DE, Mohandas N, Evans EA (1994) Molecular maps of red cell deformation: Hidden elasticity and in situ connectivity. *Science* 266(5187):1032–1035.
17. Fedosov DA, Caswell B, Karniadakis GE (2010) A multiscale red blood cell model with accurate mechanics, rheology, and dynamics. *Biophys J* 98(10):2215–2225.
18. Fischer TM (2007) Tank-tread frequency of the red cell membrane: Dependence on the viscosity of the suspending medium. *Biophys J* 93(7):2553–2561.
19. Mohandas N, Evans EA (1994) Mechanical properties of the red cell membrane in relation to molecular structure and genetic defects. *Annu Rev Biophys Biomol Struct* 23:787–818.
20. Hochmuth RM, Mohandas N, Blackshear PL, Jr. (1973) Measurement of the elastic modulus for red cell membrane using a fluid mechanical technique. *Biophys J* 13(8):747–762.
21. Waugh RE, Hochmuth RM (1987) Mechanical equilibrium of thick, hollow, liquid membrane cylinders. *Biophys J* 52(3):391–400.
22. Strey H, Peterson M, Sackmann E (1995) Measurement of erythrocyte membrane elasticity by flicker eigenmode decomposition. *Biophys J* 69(2):478–488.
23. Zhu Q, Asaro RJ (2008) Spectrin folding versus unfolding reactions and RBC membrane stiffness. *Biophys J* 94(7):2529–2545.
24. Suresh S, et al. (2005) Connections between single-cell biomechanics and human disease states: Gastrointestinal cancer and malaria. *Acta Biomater* 1(1):15–30.
25. Park Y, et al. (2008) Refractive index maps and membrane dynamics of human red blood cells parasitized by *Plasmodium falciparum*. *Proc Natl Acad Sci USA* 105(37):13730–13735.
26. Abkarian M, Faivre M, Viallat A (2007) Swinging of red blood cells under shear flow. *Phys Rev Lett* 98(18):188302.
27. Tran-Son-Tay R, Sutera SP, Rao PR (1984) Determination of red blood cell membrane viscosity from rheoscopic observations of tank-treading motion. *Biophys J* 46(1):65–72.
28. Milner ST, Safran SA (1987) Dynamical fluctuations of droplet microemulsions and vesicles. *Phys Rev A* 36(9):4371–4379.
29. Bivas I (2010) Shape fluctuations of nearly spherical lipid vesicles and emulsion droplets. *Phys Rev E Stat Nonlin Soft Matter Phys* 81(6 Pt 1):061911.
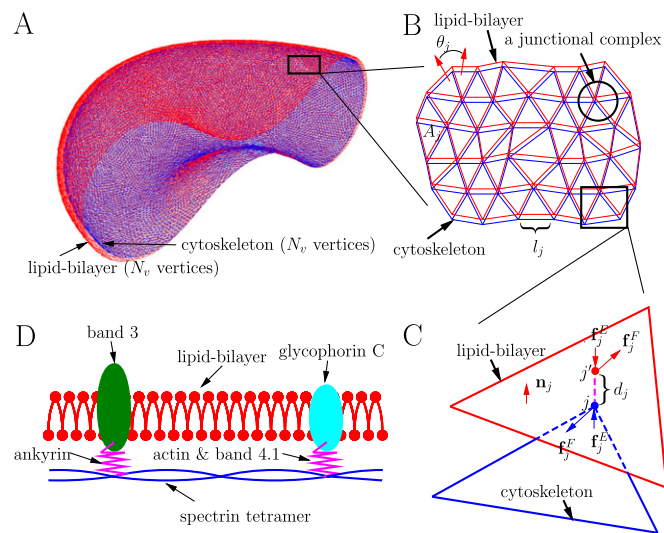
Fig. S1. (*A*) Two-component DPD model of the whole cell ($N_v = 23,867$, i.e., 23,867 DPD particles on each triangular network). (*B*) Local triangular networks of the two-component model: l_j is the spring length of the cytoskeleton; θ_j is the instantaneous angle between two adjacent triangles on the bilayer; and A_j is the triangle area. (*C*) Normal and tangential interactions between the lipid bilayer and the cytoskeleton. j' is the projection point on the lipid bilayer of vertex j on the cytoskeleton; d_j is the distance between point j and point j'; $\mathbf{f}_j^F$ is the tangential friction interaction force, whereas $\mathbf{f}_j^E$ is the normal elastic interaction force; and $\mathbf{n}_j$ is the normal direction vector of the bilayer triangle. (*D*) Physical picture of the local bilayer–cytoskeletal interaction. Although there are two kinds of interactions in each junctional complex, including the major connections via band 3 and ankyrin and the secondary connections via actin, glycophorin C, and band 4.1, we consider them together as an effective bilayer–cytoskeletal interaction in one junctional complex and model it as a normal elastic force and a tangential friction force. The vertical damping force $\mathbf{f}_j^D$ and the random force $\mathbf{f}_j^R$ are not shown for clarity.

Table S1. Main parameters of the two-component DPD model

Study cases	μ_s, pN/μm	k_c, J	η_s, Pa s	η_b, Pa s	k_{bs}, pN/μm	f_{bs}, pN·μm^{-1}·s^{-1}
Default	6	2.4e-19	0.372	0.008	46.0	0.194
Micropipette	6	2.4e-19	Independent	Independent	46.0	Independent
Fluctuations	Table S2	2.4e-19	Independent	Independent	Fig. 2A	Independent
Tank treading	6	2.4e-19	0.372	0.008	46.0	Fig. 3B
Channel flow	6	2.4e-19	Independent	Independent	46.0	Independent

μ_s, initial cytoskeleton shear stiffness (19); k_c, bilayer bending stiffness (19); η_s, cytoskeleton viscosity (27); η_b, bilayer viscosity (8, 27); k_{bs} and f_{bs}, the elastic and friction coefficients of the bilayer–cytoskeletal interactions (10).

Table S2. Shear moduli of healthy RBCs and ring-stage RBCs at the physiological and febrile temperatures obtained in ref. 25

Healthy, 37 °C, pN/μm	Healthy, 41 °C, pN/μm	Ring, 37 °C, pN/μm	Ring, 41 °C, pN/μm
6.2	4.9	14.5	20.4